ECS Transactions, 34 (1) 203-208 (2011)
10.1149/1.3567582 ©The Electrochemical Society

Robustness Enhancement in Optical Lithography: From Pixelated Mask Optimization to Pixelated Source-mask Optimization

Ningning Jia and Edmund Y. Lam

Imaging Systems Laboratory, Department of Electrical and Electronic Engineering,
The University of Hong Kong, Pokfulam Road, Hong Kong
elam@eee.hku.hk

Abstract

Optical lithography is facing a great challenge from the continuous shrinkage of industry node toward 22nm or below. The increasing sensitivity to process variations becomes a key problem hindering further progress. To address this problem, inverse lithography, which designs pixelated masks with appropriate algorithms, is favored for its capacity of exploring a larger solution space. This search capacity, however, is limited by the fixed source configuration. To this end, optimization of pixelated source and pixelated mask together has come up for further performance improvement. In this paper, a source-mask co-optimization (SMO) algorithm, which incorporates process variations into the optimization scheme, is introduced. To further improve the process robustness, we apply weighted total variation and aerial image intensity control as regularization. Simulation results show that we achieve greater pattern fidelity and enhanced process robustness by using SMO.

1 Introduction

In optical lithography, the 193nm water immersion lithography system is now on service. While further development of the shorter wavelength and higher NA (numerical aperture) is hindered for some practical reason, circuit feature size shrinkage is still continuing on the path to the ever smaller technology nodes beyond the Rayleigh resolution limit [1]. Meanwhile, printed features at small dimensions are easily affected by process variations (mainly dose and focus variations) for current low-k_1 optical lithography. Overcoming these physical limitations requires the use of computation: optimization and image processing techniques for solutions that are insensitive to process fluctuations [2]. One common approach to tackle this problem, known as optical proximity correction (OPC), makes pre-distortion on the mask topology so that the resultant circuit pattern matches the desired one [3]. Among these techniques, inverse lithography (IL) searches for a solution by solving an inverse imaging problem [4]. Compared to edge-based OPCs [5, 6], which calculate mask pre-distortion by adjusting the locations of feature edges, IL explores a wider solution space by manipulating pixels of the mask image.

Despite the theoretical ability to deliver superior wafer performance, practical implementation of inverse lithography remains a challenging task. Algorithms developed must conform to industry specifications [7], such as mask manufacturability and process robustness [8, 9]. Enhanced performance through multiple process conditions can be achieved

by incorporating process fluctuations explicitly into optimization framework [9] or by the use of cost function defined by various specifications, *e.g.*, depth of focus, process window, process variation (PV)-band, etc. [10]. However, IL alone cannot completely solve the above imaging problems. The adjustment of illumination configuration is necessary for imaging systems at $k_1 < 0.75$ [3].

Many early works have been dedicated to the development of algorithms for illumination optimization. Burkhardt *et al.* explored the diffraction orders on the pupil plane, and found the optimal source configuration to enhance image contrast for phase-shifting contact masks [11]. Socha *et al.* developed a scheme based on Hopkins partially coherent imaging equations to determine the importance of illuminator areas for periodic patterns [12]. Below 45nm circuit feature sizes, imaging using standard techniques becomes difficult. Source optimization and the reticle pattern optimization have been integrated to extend the life of current immersion lithography toolset [13]. Further degrees of freedom for optimization are provided by customized diffractive optical element (DOE) realization of the pixelated source [14]. Together with pixelated mask used in IL, the so-called free-form source-mask co-optimization fits well into the inverse lithography framework. Therefore both the source shape and its pixel intensity can be changed for an optimal source computation.

In this work, a free-form SMO scheme based on the inverse source-mask synthesis technique is proposed. The source image and the mask are iteratively updated by minimizing a cost function, which includes the regularization on the aerial image to improve the robustness against dose variation. Experimental results of SMO and mask optimization with the traditional source are compared to illustrate the robustness enhancement made by SMO.

2 Inverse Lithography with Off-axis Illuminations

Under an off-axis illumination, the aerial image (denoted by I_a) formed by the partial coherent imaging system is modeled by the Hopkins equation [15]. The image intensity at (x, y) is given by

$$\begin{aligned} I_a(x,y) &= \int_{-\infty}^{\infty}\!\!\cdots\int J(f,g)\hat{H}(f+f',g+g')\hat{H}^{\dagger}(f+f'',g+g'')\hat{M}(f',g')\hat{M}^{\dagger}(f'',g'') \\ &\quad \times \mathrm{e}^{-i2\pi[(f'-f'')x+(g'-g'')y]}\,\mathrm{d}f\,\mathrm{d}g\,\mathrm{d}f'\,\mathrm{d}g'\,\mathrm{d}f''\,\mathrm{d}g'', \end{aligned} \tag{1}$$

where $\hat{H}$ and $\hat{H}^{\dagger}$ denote the pupil function (optical transfer function, OTF) and its complex conjugate, respectively. $\hat{M}$ represents the mask spectrum. J is the source function, which is represented by a pixelated image, with each pixel denoting one discrete source point. A single source point gives rise to a projected image, and the collection of images from all source points contributes to $I_a(x, y)$.

As stated in [16], inverse lithography computes the mask pattern by solving an optimization problem. The solution can be obtained by minimizing a cost function, which has a general form of

$$\begin{aligned} M_{\mathrm{opt}}(x,y) &= \arg\min_{M(x,y)} \mathcal{D}\left\{\Gamma\{I_a(x,y)\}, \hat{I}(x,y)\right\} \\ &\quad \text{subject to} \quad M(x,y) \in \{0,1\}. \end{aligned} \tag{2}$$

In the above equation, $M(x, y)$ represents the binary pattern on the mask and $I(x, y)$ is the target design, which is the desired pattern on the wafer. $\Gamma(\cdot)$ is the function approximating the photo-resist effect, which can be modeled as a soft thresholding by a logarithmic sigmoid function [8]. For IL optimization, the measure of closeness between the printed pattern and

the desired circuit is not limited to a unique form. Here we denote it by $\mathcal{D}$ in general. A common method refers to the use of ℓ_1 or ℓ_2 norm in the form of $\|\Gamma\{I_a(x,y)\} - \hat{I}(x,y)\|$, which is regarded as the pattern fidelity term. Other than this, measure $\mathcal{D}$ may also include terms such as depth of focus (DOF), normalized image log slope (NILS), manufacturability, etc., which are called regularization terms.

3 Free-form Source and Mask Co-optimization

The source function J is fixed during optimization in IL. For SMO, both the source and the mask are variables to be optimized. The optimization problem described in Equation (2) then becomes

$$\begin{aligned} \{M_{\text{opt}}(x,y), J_{\text{opt}}(f,g)\} &= \arg\min_{\{M,J\}} \mathcal{D}\left\{\Gamma\{I_a(x,y)\}, \hat{I}(x,y)\right\} \\ &\quad \text{subject to} \quad M(x,y) \in \{0,1\}, \quad J(f,g) \geq 0. \end{aligned} \tag{3}$$

Note that the source $J(f,g)$ takes nonnegative value, and is normalized by its total energy.

To enhance the process robustness, we explicitly add process variations into Equation (3). As in [9], focus and dose variations are first considered as random variables, and then a set of samples are taken to form the training set. Under the process conditions determined by the training set, J and M are iteratively updated to find the optimal solutions.

Meanwhile, to enhance the image contrast, we apply the total variation (TV) regularization, since the aerial image is piecewise smooth. To maintain the edge sharpness and avoid oversmoothing small features, a weight matrix based on the edge of the target image is added as a control of the strength of TV minimization. The weight matrix takes small values at the edge, where gradients are large, and it takes relatively large values elsewhere.

Other than giving the edge smaller smooth penalty, the image contrast can be further improved by adding another regularization term that manipulates the intensity of the aerial image. Here we choose to minimize $\|I_a(x,y) - t\hat{I}(x,y)\|_2^2$ at the edge, which means a weighted mean square error is minimized. The weight matrix is determined by the target image's edge, and $\frac{t}{2}$ is the threshold used in the photo-resist model. This penalty forces the intensities at the edge to reach a lower bound 0 when the phase of the target design is 0°, and an upper bound t when the phase is 180°. Thus intensities in the vicinity of the threshold are equally penalized. Since we minimize across multiple defocus conditions, it also helps to improve the depth of focus. The proposed form of $\mathcal{D}\left\{\Gamma\{I_a(x,y)\}, \hat{I}(x,y)\right\}$ is then given by

$$\begin{aligned} \mathcal{D}\left\{\Gamma\{I_a(x,y)\}, \hat{I}(x,y)\right\} &= \sum_{x,y}\left(\Gamma\{I_a(x,y)\} - \hat{I}(x,y)\right)^2 + \lambda_1 \sum_{x,y}\left|W_1(x,y)\nabla I_a(x,y)\right| \\ &\quad + \lambda_2 \sum_{x,y} W_2(x,y)\left(I_a(x,y) - t\hat{I}(x,y)\right)^2 \\ &= \mathcal{J}\left\{\Gamma\{I_a\}, \hat{I}\right\} + \lambda_1 \mathcal{R}_{\text{TV}}\{I_a\} + \lambda_2 \mathcal{R}_{\text{aerial}}\{I_a\}. \end{aligned} \tag{4}$$

The measure $\mathcal{D}$ is composed of three terms, which relate to pattern fidelity ($\mathcal{J}$), TV regularization ($\mathcal{R}_{\text{TV}}$) and aerial image regularization ($\mathcal{R}_{\text{aerial}}$). The weight matrix of TV regularization and the aerial image penalty are denoted by W_1 and W_2, respectively.

In fact, $\|I_a(x,y) - \hat{I}(x,y)\|_2^2$ has been used as the fidelity term in [17], which also claimed that using $\|\Gamma\{I_a(x,y)\} - \hat{I}(x,y)\|_2^2$ would lead to further decrease of the pattern error. Note that the upper bound of the aerial image intensity over the whole image is difficult to

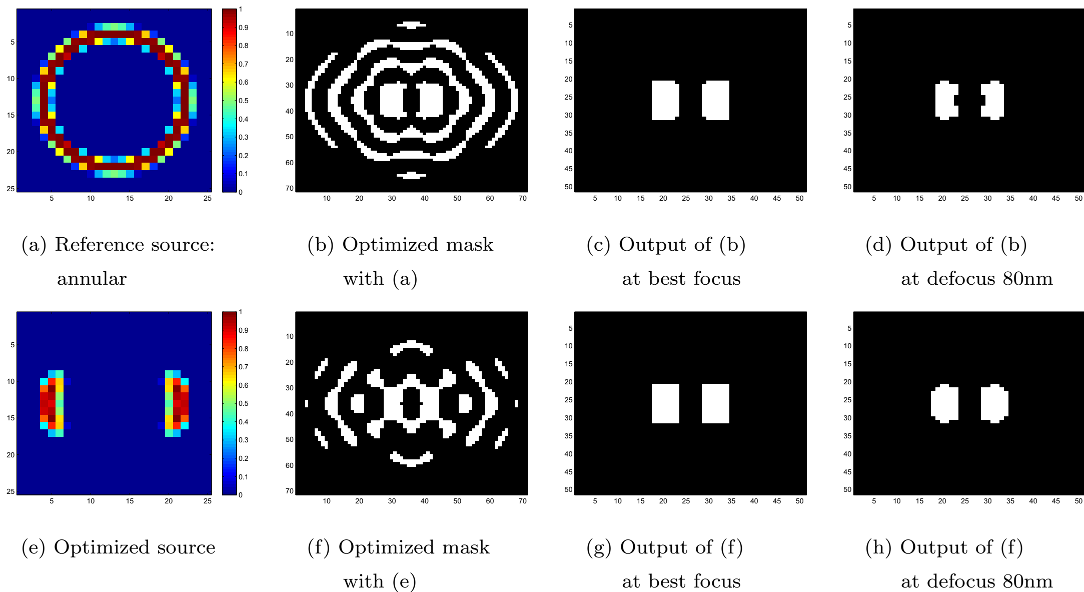

(a) Reference source: annular
(b) Optimized mask with (a)
(c) Output of (b) at best focus
(d) Output of (b) at defocus 80nm
(e) Optimized source
(f) Optimized mask with (e)
(g) Output of (f) at best focus
(h) Output of (f) at defocus 80nm

Figure 1: Results of reference source and SMO.

predict. Sometimes it might exceeds the target image intensity 1. Our penalty has no such concern, because it applies only on intensities near the edge that are mostly quite close to the threshold. With the fidelity term $\mathcal{J}$ minimizing the pattern error, $\mathcal{R}_{\text{TV}}$ and $\mathcal{R}_{\text{aerial}}$ help to enhance the process robustness further.

4 Results

We apply SMO on a target pattern with two rectangles, and compare the results with a reference annular source. The critical dimension of the test pattern is 50nm, which is the distance between two rectangles. The width of each rectangle is 60nm and length 110nm, with the mask pixel size $10 \times 10\text{nm}^2$. The image matrix size is 151×151. In the following we show truncated images for a clearer demonstration.

In Figure 1, the first row (figure (a), (b), (c) and (d)) displays the reference source, the optimized mask, the output at best focus and defocus, respectively. Following the same structure, the second row shows results of SMO. One can observe that, although the printed patterns in Figure 1 (c) and (g) show similar performance at best focus, the image quality of Figure 1 (d) deterioates more than that of Figure 1 (h) at a defocus 80nm.

To quantitatively exam the performance of SMO, we draw process windows [3] of the reference source and the optimized source. Four critical locations, which are numbered and marked with different colors in Figure 2 (a), are chosen for the process window calculation. To be specific, the width and length of the rectangle, as well as the space between two rectangles, are measured. Figure 2 (b) and (c) are calculated process windows for the reference source and SMO, respectively. In each figure there are four pairs of curves drawn by four different colors that are consistent with the colors used in Figure 2 (a). Each pair of curves with the same color represents the maximum doses and the minimum doses, between which the corresponding feature keeps its nominal size over the measured focus range. And the area bounded by the four pairs of curves defines the process window. The dose range specified by the maximum dose and the minimum dose is the exposure latitude [3]. One can observe that process window in Figure 2 (c) is larger than that in Figure 2 (b). For instance,

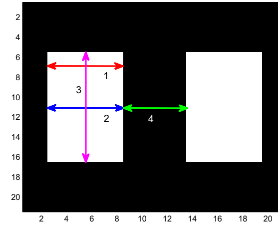

(a) Measured locations

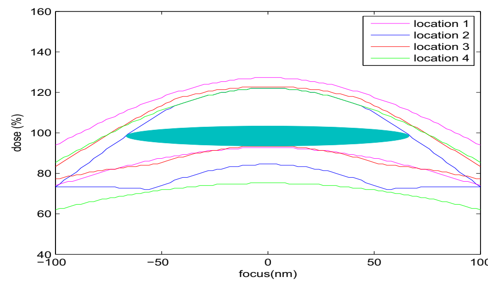

(b) Process window of source (a)

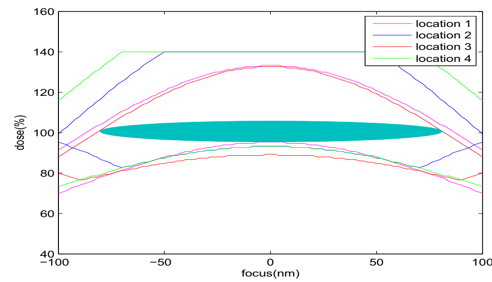

(c) Process window of source (e)

Figure 2: Process window.

with a 10% exposure latitude, (c) exhibits a larger focus range than (b), as illustrated by the ellipses in (b) and (c). Thus the process robustness is enhanced by SMO. In addition, the optimized illumination configuration in this case is quite like a dipole source, which indicates that one can use the result of free-form SMO for parametric source optimization [18].

5 Conclusion

In this paper, we compare the performance of free-form source-mask co-optimization with that of pixelated mask design with a fixed traditional illumination. Experimental results show that SMO improves the printed pattern fidelity across multiple process conditions. Thus it enhances the process robustness. Further interest focuses on SMO for multiple circuit patterns and developing faster SMO algorithms.

Acknowledgments

This work was supported in part by the Research Grants Council of the Hong Kong Special Administrative Region, China, under Projects HKU 7134/08E, and by the UGC Areas of Excellence project *Theory, Modeling, and Simulation of Emerging Electronics*.

References

[1] M. Rothschild, "A roadmap for optical lithography," *Opt. Photonics News*, vol. 21, pp. 26–31, Jun. 2010.

[2] E. Y. Lam, "Regularization in inverse lithography: Enhancing manufacturability and robustness to process variations," in *China Semiconductor Technology International Conference (CSTIC)*, vol. 27 of *ECS Transactions*, pp. 427–432, 2010.

[3] A. K. Wong, *Resolution Enhancement Techniques in Optical Lithography*. Washington: SPIE, 2001.

[4] L. Pang, Y. Liu, and D. Abrams, "Inverse lithography technology (ILT): A natural solution for model-based SRAF at 45nm and 32nm," in *Photomask and Next-Generation Lithography Mask Technology XIV* (H. Watanabe, ed.), vol. 6607 of *Proc. SPIE*, p. 660739, 2007.

[5] J. Mitra, P. Yu, and D. Z. Pan, "RADAR: RET-aware detailed routing using fast lithography simulations," in *42nd Design Automation Conference*, pp. 369–372, 2005.

[6] A. Gu and A. Zakhor, "Optical proximity correction with linear regression," *IEEE Trans. Semicond. Manuf.*, vol. 21, pp. 263–271, May 2008.

[7] E. Y. Lam and A. K. Wong, "Computation lithography: Virtual reality and virtual virtuality," *Opt. Express*, vol. 17, pp. 12259–12268, Jul. 2009.

[8] A. Poonawala and P. Milanfar, "Mask design for optical microlithography — an inverse imaging problem," *IEEE Trans. Image Process.*, vol. 16, pp. 774–788, Mar. 2007.

[9] N. Jia and E. Y. Lam, "Machine learning for inverse lithography: Using stochastic gradient descent for robust photomask synthesis," *J. Opt.*, vol. 12, p. 045601, Apr. 2010.

[10] D. S. Abrams and L. Pang, "Fast inverse lithography technology," in *Optical Microlithography XIX* (D. G. Flagello, ed.), vol. 6154 of *Proc. SPIE*, p. 61541J, 2006.

[11] M. Burkhardt, A. Yen, C. Progler, and G. Wells, "Illuminator design for the printing of regular contact patterns," *Microelectron. Eng.*, vol. 41–42, pp. 91–96, Mar. 1998.

[12] R. Socha, M. Eurlings, F. Nowak, and J. Finders, "Illumination optimization of periodic patterns for maximum process window," *Microelectron. Eng.*, vol. 61–62, pp. 57–64, Jul. 2002.

[13] K. Tian *et al.*, "Benefits and trade-offs of global source optimization in optical lithography," in *Optical Microlithography XXII* (H. J. Levinson and M. V. Dusa, eds.), vol. 7274 of *Proc. SPIE*, p. 72740C, 2009.

[14] K. Lai *et al.*, "Experimental result and simulation analysis for the use of pixelated illumination from source mask optimization for 22nm logic lithography process," in *Optical Microlithography XXII* (H. J. Levinson and M. V. Dusa, eds.), vol. 7274 of *Proc. SPIE*, p. 72740A, 2009.

[15] A. K. Wong, *Optical Imaging in Projection Microlithography*. Washington: SPIE, 2005.

[16] L. Pang, Y. Liu, and D. Abrams, "Inverse lithography technology (ILT), what is the impact to photomask industry?" in *Photomask and Next-Generation Lithography Mask Technology XIII* (M. Hoga, ed.), vol. 6283 of *Proc. SPIE*, p. 62830X, 2006.

[17] A. Poonawala and P. Milanfar, "Double-exposure mask synthesis using inverse lithography," *J. Micro/Nanolith. MEMS MOEMS*, vol. 6, p. 043001, Oct. 2007.

[18] Y. Deng, Y. Zou, K. Yoshimoto, Y. Ma, C. E. Tabery, J. Kye, L. Capodieci, and H. J. Levinson, "Considerations in source-mask optimization for logic applications," in *Optical Microlithography XXIII* (M. V. Dusa and W. Conley, eds.), vol. 7640 of *Proc. SPIE*, p. 76401J, 2010.